Beam Size, Shape and Efficiencies for the ATNF Mopra Radio Telescope at 86–115 GHz

Ned Ladd[A,D]*, Cormac Purcell*[B,D]*, Tony Wong*[B,C]*, and Stuart Robertson*[C]

[A] Physics Department, Bucknell University, Lewisburg PA 17837, USA
[B] School of Physics, University of New South Wales, Sydney NSW 2052, Australia
[C] CSIRO Australia Telescope National Facility, Epping NSW 1710, Australia
[D] Corresponding authors. Email: ladd@bucknell.edu; crp@phys.unsw.edu.au

Abstract: We present data characterising the performance of the Mopra Radio Telescope during the period 2000–2004, including measurements of the beam size and shape, as well as the overall beam efficiency of the telescope. In 2004 the full width half maximum of the beam was measured to be $36 \pm 3''$ at 86 GHz, falling to $33 \pm 2''$ at 115 GHz. Based on our observations of Jupiter we measured the beam efficiency of the Gaussian main beam to be 0.49 ± 0.03 at 86 GHz and 0.42 ± 0.02 at 115 GHz. Sources with angular sizes of $\sim 80''$ couple well to the main beam, while sources with angular sizes between $\sim 80''$ and $\sim 160''$ couple to the both the main beam and inner error beam. Measurements indicate that the inner error beam contains approximately one-third the power of the main beam. We also compare efficiency corrected spectra to measurements made at similar facilities and present standard spectra taken towards the molecular clouds Orion-KL and M17-SW.

Keywords: instruments — interstellar: molecules — radio sources: lines

1 Introduction

The Mopra Observatory is a 22-m telescope operated by the Australia Telescope National Facility (ATNF), and located at the edge of the Warrumbungle Mountains near Coonabarabran, NSW, and the optical observatories on nearby Siding Spring Mountain. The telescope's longitude is $149°5'58''$, its latitude is $31°16'58''$, and its altitude is 866 m. The facility is equipped with receivers for observations at wavelengths ranging from 20 cm to 3 mm, with backends capable of spectral line observations of varying bandwidth and frequency resolution. For a more complete description of the technical capabilites of the facility, see `www.narrabri.atnf.csiro.au/mopra`.

Three-millimetre wavelength observing is generally conducted during the winter months (June–September) when atmospheric water vapour levels typically reach their minimum annual values. Observations are made with a dual polarisation SIS receiver (Moorey et al. 1997) which produces a 600-MHz instantaneous bandwidth tunable between 86 and 115 GHz. The receiver output is analysed with a flexible correlator (Wilson et al. 1992) which can be configured for bandwidths between 4 and 256 MHz within the receiver's 600-MHz window. Calibration of spectra onto an antenna temperature (T_A^*) scale is accomplished using a single ambient temperature load inserted into the receiver beam.

In this paper, we present spectral line and continuum measurements of celestial sources in an effort to characterise the size and shape of the system's primary beam and inner sidelobes, as well as the contribution to the measured power from a large angle error beam. From these data, we measure the overall efficiency of the antenna, and how this efficiency varies with observing frequency and source angular size. Using data from previous observing seasons, we measure how the telescope efficiency varied with time from the 2000 observing season to the present. Lastly, we present standard spectra for well-known sources in various molecular lines.

2 Beam Mapping Observations

Complete maps of the telscope's beam were obtained during the 2003 and 2004 observing seasons. We mapped the beam using the SCAN mode of the TCS observing software, where the telescope was driven at constant angular speed in Right Ascension while data were acquired. The angular speed and integration time for each data sample were adjusted to ensure that the resulting map was not smeared due to the scanning motion. Each beam map consisted of several SCANed rows, each separated in Declination by $10''$.

We mapped the 86.243 GHz SiO ($J = 2 \rightarrow 1$, $v = 1$) maser emission from several evolved stars, as well as the continuum emission from the planets Mercury, Mars, and Jupiter. The SiO maser observations produced high signal-to-noise ratio (SNR) maps, primarily because baselining the spectral line data provides for excellent cancellation of variable contribution from atmospheric emission; however, these maps provide information regarding the structure of the beam only at the 86 GHz frequency. We mapped the continuum emission from planets at a variety

Table 1. SiO masers mapped

| Source	R.A. (J2000.0) [hms]	Dec (J2000.0) [dms]	Date observed	Frequency [GHz]	Map extent [$'' \times ''$]
O Ceti (Mira)	02 : 19 : 20.7	−02 : 58 : 38	2003 Aug 18 17 : 18	86.2	110 × 120
O Ceti (Mira)	02 : 19 : 20.7	−02 : 58 : 38	2003 Aug 18 18 : 33	86.2	110 × 120
O Ceti (Mira)	02 : 19 : 20.7	−02 : 58 : 38	2003 Aug 19 17 : 34	86.2	110 × 120
O Ceti (Mira)	02 : 19 : 20.7	−02 : 58 : 38	2003 Aug 19 19 : 02	86.2	110 × 120
O Ceti (Mira)	02 : 19 : 20.7	−02 : 58 : 38	2003 Aug 20 17 : 11	86.2	110 × 120
O Ceti (Mira)	02 : 19 : 20.7	−02 : 58 : 38	2003 Aug 20 18 : 23	86.2	110 × 120
W Hya	13 : 49 : 29.4	−28 : 22 : 03	2003 Oct 21 03 : 36	86.2	110 × 120
W Hya	13 : 49 : 29.4	−28 : 22 : 03	2003 Oct 21 05 : 25	86.2	110 × 120
IK Tau	03 : 53 : 53.2	11 : 24 : 23	2003 Oct 22 15 : 15	86.2	110 × 120
Orion	05 : 35 : 38.6	−05 : 22 : 30	2003 Oct 22 16 : 56	86.2	110 × 120
Orion	05 : 35 : 38.6	−05 : 22 : 30	2003 Oct 22 18 : 08	86.2	110 × 120
AH Sco	17 : 12 : 04.2	−32 : 19 : 32	2003 Oct 23 07 : 02	86.2	170 × 180
VY CMa	07 : 23 : 42.5	−25 : 46 : 02	2003 Oct 23 20 : 21	86.2	170 × 180
R Leo	09 : 48 : 14.3	11 : 25 : 44	2003 Oct 23 21 : 44	86.2	170 × 180
W Hya	13 : 49 : 29.4	−28 : 22 : 03	2003 Oct 24 00 : 11	86.2	170 × 180
R Leo	09 : 48 : 14.3	11 : 25 : 44	2003 Oct 24 19 : 18	86.2	170 × 180
R Leo	09 : 48 : 14.3	11 : 25 : 44	2003 Oct 24 21 : 41	86.2	170 × 180

Table 2. Planetary observations

| Source	Date observed [UT]	Angular size [$''$]	Frequency #1 [GHz]	Frequency #2 [GHz]	Map extent [$'' \times ''$]
Mars	2003 Oct 20 1110	16.9	100	86	110 × 70
Mars	2003 Oct 22 1230	16.5	100	86	130 × 120
Mars	2003 Oct 22 1405	16.5	100	86	90 × 80
Mars	2003 Oct 23 1015	16.4	100	86	200 × 180
Mars	2003 Oct 23 1205	16.4	100	86	200 × 180
Mars	2003 Oct 23 1335	16.4	100	86	200 × 180
Mercury	2004 Jun 4 2308	5.7	110	86	130 × 120
Mercury	2004 Jun 4 2345	5.7	110	86	130 × 120
Mercury	2004 Jun 5 2245	5.7	99	99	130 × 120
Mercury	2004 Jun 5 2315	5.6	99	99	130 × 120
Mercury	2004 Jun 6 0028	5.6	115	115	130 × 120
Mercury	2004 Jun 6 0058	5.6	115	115	130 × 120
Mercury	2004 Jun 6 0200	5.6	99	86	130 × 120
Mercury	2004 Jun 6 0230	5.6	99	86	130 × 120
Jupiter	2004 Jun 5 0836	36.4	115	86	130 × 120
Jupiter	2004 Jun 5 0913	36.4	115	86	130 × 120
Jupiter	2004 Jun 5 1007	36.4	86	86	130 × 120
Jupiter	2004 Jun 6 0523	36.3	99	99	130 × 120
Jupiter	2004 Jun 6 0551	36.3	99	99	130 × 120
Jupiter	2004 Jun 6 0704	36.3	99	99	130 × 120
Jupiter	2004 Jun 6 0802	36.3	115	115	130 × 120
Jupiter	2004 Jun 6 0833	36.3	115	86	130 × 120

of frequencies throughout the tuning range of the telescope's receiver, and these data show how the telescope beam changes as a function of frequency; however the SNR of these maps is worse than that for the SiO maser maps because it is more difficult to account for variations in atmospheric emission in continuum mode. Tables 1 and 2 display the characteristics of the SiO maser and planet mapping observations. In particular Table 1 presents the SiO maser coordinates, map extent, and observation date, while Table 2 includes additional information on the planetary angular size and observing frequency. We constructed

high SNR beam maps from these observations by transforming each SCAN map onto an altitude–azimuth grid co-moving with the source. The data were then coadded to form the maps shown in Figures 1, 2, and 3.

The data presented in Figure 1 comprise the highest SNR measurements of the telescope beam shape during the 2003 and 2004 seasons. During both seasons the beam was quite round to the 20% level, but at lower levels, particularly during the 2003 season, there existed an error beam of relatively large angular size. The 2003 data show that this error beam was asymmetric in azimuth, and it was
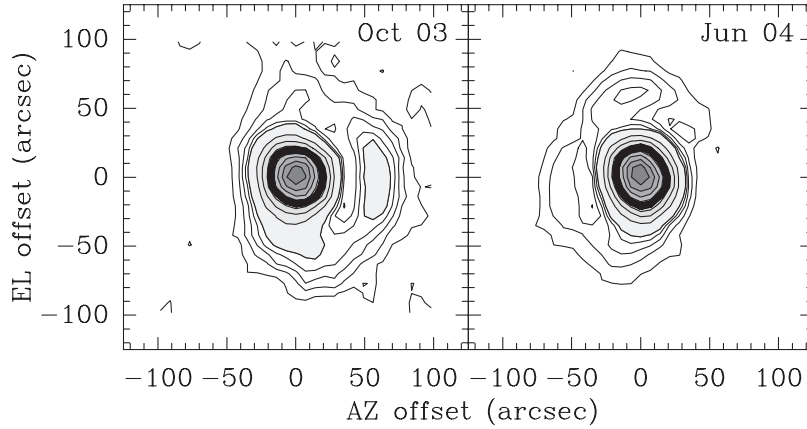
Figure 1   Maps of the telescope beam constructed from 86 GHz SiO maser emission data taken in 2003 October (left panel) and 2004 June (right panel). Contours and greyscales increment from 1% to 10% of peak intensity in 1% intervals, and then from 10% to 90% in 10% intervals. The 50% contour is plotted in bold. The substantial change in the beam response at low levels is due to a translational shift in the position of the telescope's subreflector accomplished in 2004 May.
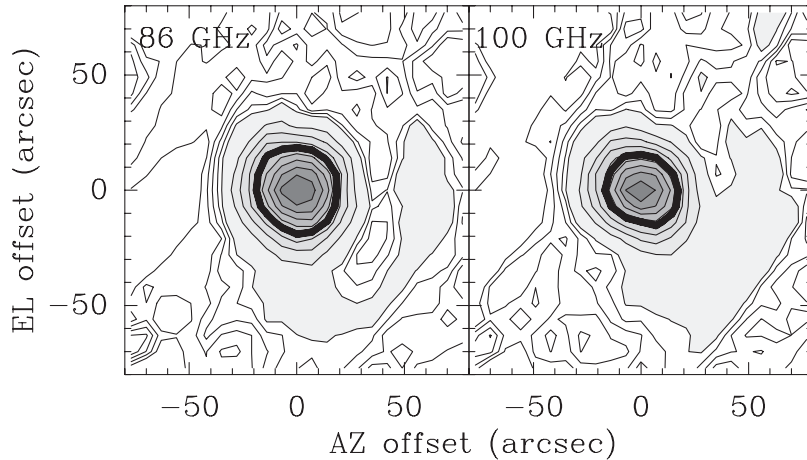
Figure 2   Maps of the telescope beam constructed from continuum observations of Mars taken in 2003 October at 86 GHz (left panel) and 100 GHz (right panel). Contours and greyscales increment from 1% to 10% of peak intensity in 1% intervals, and then from 10% to 90% in 10% intervals. The 50% contour is plotted in bold.

determined that the telescope's subreflector was not well aligned with the receiver optical axis. The subreflector was moved in 2004 May, and the data taken in 2004 June show a substantial decrease in both the amplitude and the angular size distribution of the error beam. The movement of the subreflector also resulted in a measurable improvement in the efficiency of the telescope, as discussed below.

Figure 2 shows the structure of the 2003 beam derived from continuum observations of Mars. Strictly speaking, these maps depict the beam convolved with the planet's disk, but for these observations, the angular size of Mars was considerably smaller than the full width at half maximum (FWHM) size of the telescope's beam (see Table 2). The broadening of the mapped profile due the angular extent of Mars is very small ($\lesssim$10% of the FWHM contour), and these maps show the same beam structure seen in the 2003 SiO maser observations (Figure 1, left panel), including the asymmetric error lobe. Though these data are noisier than the SiO maser results, it is clear that the

angular size of the FWHM beam decreases with increasing frequency.

Figure 3 shows the continuum maps made during the 2004 season. Mercury had a very small angular size ($\sim$6″) during the observations, and so structure seen in the maps of this source (left panels) is due entirely to the telescope beam. However, because of the small angular size of Mercury, emission from this source was strongly beam-diluted, and the SNR of the resulting maps is relatively low. Nonetheless, the expected decrease of FWHM beam size with increasing frequency is quite obvious.

The right panels of Figure 3 contain maps of Jupiter at 86, 99, and 115 GHz. Jupiter's angular size ($\sim$36″) was comparable to the FWHM size of the telescope beam, and so the structure in these maps is broader than telescope's beam. Consequently, the change in FWHM beam size with increasing frequency is less obvious. The low-level beam structure, however, is better mapped with the Jupiter observations because this source is much brighter than Mercury.
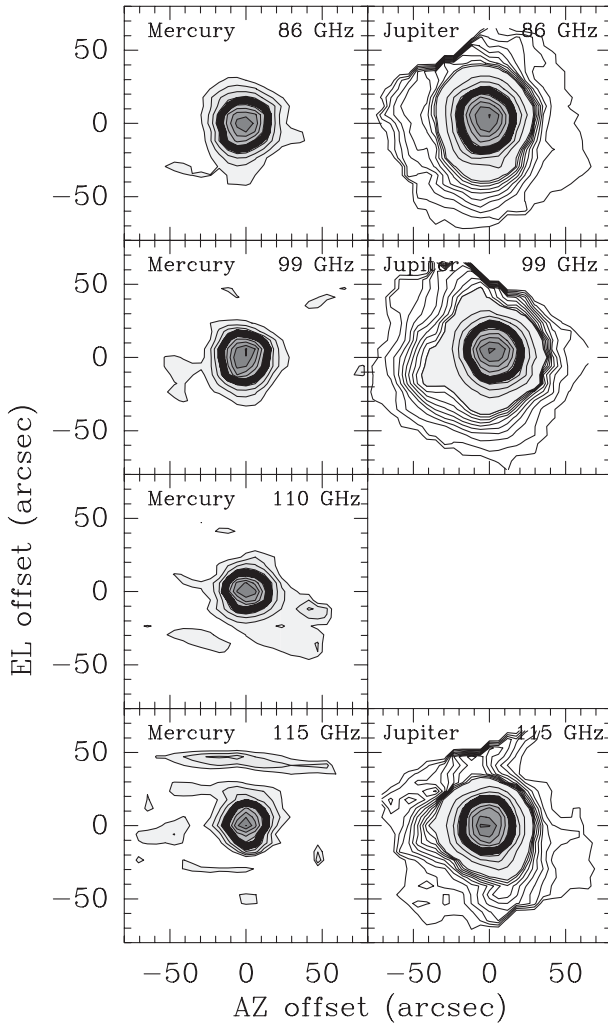
Figure 3 Maps of the telescope beam constructed from continuum observations of Mercury (left panels) and Jupiter (right panels) taken in 2004 June at 86, 99, 110, and 115 GHz. In all maps, the greyscales range from 10% to 90% of peak intensity in 10% intevals. The Jupiter maps also contain unshaded contours which range from 1% to 10% of peak intensity in 1% increments. The 50% contour is plotted in bold.

Table 3. FWHM beam sizes from SiO maser and planetary observations

Year	Frequency [GHz]	FWHM [″]
2003	86	37 ± 1
	100	35 ± 4
2004	86	36 ± 3
	100	36 ± 3
	115	33 ± 2

To measure the FWHM beam size at each frequency, we modelled the main beam as a two dimensional Gaussian, and fitted the individual SCAN maps with either the Gaussian function (for the SiO maser data) or the Gaussian convolved with a disk of appropriate angular size (for the planet maps). Because of their low SNR, the 2004 Mercury data (Figure 3) produced poorly constrained FWHM
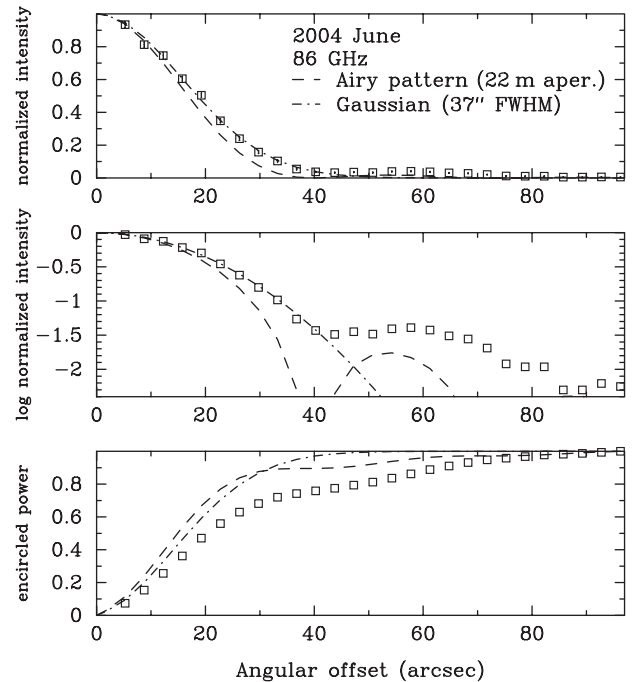
Figure 4 The azimuthally averaged radial beam profile obtained in 2004 June from SiO maser observations. The top panel shows the normalised intensity as a function of radial offset in arcseconds. The centre panel shows the logarithm of the normalised intensity as a function of radial offset. In both panels, the dotted line describes the Airy profile expected from a fully illuminated 22-m aperture, and the dot-dash line describes the profile from a Gaussian profile with FWHM of 37″. The bottom panel shows the encircled power as a function of angular size for the data, the Airy profile, and the Gaussian profile. The encircled energies are all normalised to unity for an angular radius of 96″ (i.e. the extent of the beam map).

values; however, the 2004 Jupiter maps were well-fitted with a Gaussian plus planetary disk model, and produced well-constrained FWHM size estimates. Typical 1σ uncertainties in the fitted FWHM sizes from both the 2004 Jupiter data and the 2003 Mars data were 5–10″. A weighted average of the fitted values for each SCAN map at each frequency yielded overall best-fit FWHM beam sizes with typical uncertainties of 3″. Table 3 lists the calculated values, which range from 33″ to 37″.

The azimuthally-averaged 86 GHz radial beam profile from the 2004 SiO maser data is shown in Figure 4. These data clearly show the separation of the beam into a central 'core' beam and the extended error beam. At 86 GHz, the central 'core' beam is well-fit by a Gaussian with FWHM size of 37″ out to intensities of less than 5% of peak and an angular offset of ∼40″. The error beam extends to ∼80″ with an average intensity of slightly less than 2%. The core beam within 40″ accounts for 75% of the total power detected within 96″ of the beam centre, while the remaining 25% lies in the error beam between 40″ and 96″.

2.1 Beam Efficiency

Based on the measured beam profiles, we divide the telescope's response into three components: (a) a circular 'main beam' with a Gaussian profile which extends to

angular offsets of $40''$, (b) an 'inner error beam' which extends from offsets of $40''$ to $80''$, and (c) an 'outer error beam' which has low intensity but may extend to large offset angles. (The observations presented here are not sensitive to the outer error beam, because all SCANs were referenced to an 'off' position only 5–$15'$ from the map centre.) The presence of a substantial inner error beam complicates calibration, and in general implies that the telescope efficiency will depend on the angular size of the target source.

Sources of small angular size ($\Theta \leq 80''$) will couple well to the main beam but not to either of the error beams. In this case, the measured antenna temperature T_A^* will depend on the source intensity distribution $T_R(\phi)$ as a function of offset angle ϕ, and its coupling to the Gaussian main beam $P_{mb}(\phi)$ as follows:

$$T_A^* = \eta_{mb} \frac{\int T_R(\phi) P_{mb}(\phi) d\Omega}{\int P_{mb}(\phi) d\Omega} \qquad (1)$$

where η_{mb} is the main beam efficiency which quantifies the fraction of the total measured power contained in the main beam,

$$\eta_{mb} \equiv \frac{\int P_{mb}(\phi) d\Omega}{\int_{2\pi} P_b(\phi) d\Omega} \qquad (2)$$

$P_b(\phi)$ is the response of the telescope beam as a function of solid angle, and the integration is taken over the forward hemisphere (see Kutner & Ulich 1981 and Mangum 1993 for more details, including a discussion of the various temperature scales).

In principle, one can measure η_{mb} with observations of any source with a known intensity distribution, but most commonly used sources are planets because their intensities and sizes are well known. The 2003 and 2004 planetary measurements at 86 and 100 GHz were conducted when the planets had an angular sizes of 5–$35''$, so the emission coupled well to the core beam, but not to the error beam. Ulich (1981) produced models for the 3-mm brightness temperatures of Mars and Jupiter. The brightness temperature of Jupiter is constant at this frequency, but because the orbit of Mars is eccentric, the brightness temperature for that planet varies with its heliocentric distance. This model is consistent with more detailed models of martian emission based on Mars orbiter and lander data (Neugebauer et al. 1971), and has been used for calibration of other millimetre-wave telescopes (Mangum 1993). The disk-averaged brightness temperature of Mercury is more complicated, depending not only on heliocentric distance but also phase angle, since the Sun-facing side of Mercury is significantly warmer than its shadowed hemisphere. Consequently, models for Mercury's brightness temperature variation (Epstein & Andrew 1985) are more poorly constrained and this object is a less reliable calibrator. Therefore, we chose to use our Mars data to determine η_{mb} for the 2003 season, and our Jupiter data to determine η_{mb} for the 2004 season. Assuming that both Mars and Jupiter are circular disks with brightness temperatures given by Ulich's (1981) model, we measure the main beam

Table 4. **Main beam efficiencies η_{mb}**

Frequency [GHz]	2003	2004
86	0.39 ± 0.02	0.49 ± 0.03
100	0.37 ± 0.02	0.44 ± 0.03
115		0.42 ± 0.02

efficiencies and these are given in Table 4. The listed uncertainties in each value are the standard error in the mean of the values obtained from each beam map. Two trends are evident from the data. Firstly, for each observing season, η_{mb} varies inversely with frequency, as expected for any reflecting surface. Secondly, the 2004 main beam efficiency at all frequencies is substantially larger than the 2003 values. This improvement of approximately 25% in the values is a direct result of the subreflector repositioning in 2004 May.

Sources with angular diameters larger than $\sim 80''$ require a more complicated calibration because these source intensity distributions will also couple to the inner error beam. Using the same methodology outlined above for estimation of η_{mb}, we can write an expression for the antenna temperature measured for a larger source as a function of the extended beam, P_{xb}, which includes the contributions of both the main and inner error beam, as a function of the extended beam efficiency, η_{xb}, as follows:

$$T_A^* = \eta_{xb} \frac{\int T_R(\phi) P_{xb}(\phi) d\Omega}{\int P_{xb}(\phi) d\Omega} \qquad (3)$$

where η_{xb} is the main beam efficiency which quantifies the fraction of the total measured power contained in the extended beam,

$$\eta_{xb} \equiv \frac{\int P_{xb}(\phi) d\Omega}{\int_{2\pi} P_b(\phi) d\Omega}. \qquad (4)$$

Though we have no direct measurements of the beam efficiency for sources of this angular size, we can estimate the beam efficiency from our knowledge of the beam profile. The Jupiter measurements indicate that 42–49% of the total power collected by the telescope in the forward direction is contained in the main beam. Further, the 86 GHz beam radial profiles indicate that the inner error beam contains approximately one-third of the power contained in the main beam. Therefore, we conclude that the fraction of the total power contained in the main and inner error beams is $\sim$55–65%. We estimate $\eta_{xb} = 0.65$ at 86 GHz and and $\eta_{xb} = 0.55$ at 115 GHz for a source which couples well to the main and inner error beams. Though the 2003 values for η_{mb} were substantially lower than the 2004 values, the relative contribution from the inner error beam was larger. Our 2003 radial beam profiles indicate that the ratio of power in the main beam to power in the inner error beam was 2:1 (rather then a 3:1 for the 2004 observations). Therefore, we estimate that η_{xb} during the 2003 season was not much smaller than the 2004 season value (perhaps 0.5–0.6 rather than 0.55–0.65). This result indicates

that the substantial improvement in the 2004 η_{mb} values was accomplished by concentrating the inner error beam power into the main beam, and that the outer error beam was probably little changed by the 2004 May subreflector movement.

The values for η_{xb} are likely comparable to, but less than, the values for η_{fss}, the forward scattering and spillover efficiency. This latter value is usually determined from observations of sources with larger angular sizes, such as the Moon ($\Theta = 1800''$), and so includes contributions from the outer error beam on larger angular scales. The beam maps presented here were constructed using reference observations located only a few arcminutes away from the source position ($6'$ for the Mars observations and $15'$ for the SiO maser observations) so they contain no information on the power at these large angular scales.

3 Gain History

In an effort to improve system sensitivity and beam shape, the dish surface and subreflector position were adjusted several times between 1999 and 2004. Successive rounds of panel settings based on holography at 30 GHz have reduced the RMS error on the surface from 270 μm in 1999 to 180 μm in 2004. The telescope was also collimated by moving the subreflector with respect to the optical axis, leading to a more symmetrical beam shape and an increase in the fraction of the total power present in the main beam.

The telescope focus was set at the start of each observing season by scanning the beam across a bright SiO maser and measuring the beam profile at 86 GHz. Several focus positions were evaluated in this manner and the position of highest recieved power and smallest angular profile was taken to be the optimum focus point. The beam size and therefore the gain depend on the accuracy of the focus achieved.

Table 5 lists the changes made to the telescope in chronological order from 2000 to 2004. All changes, except for one panel setting during 2003 August, occurred outside of the normal 3-mm observing season. Our data show that the 2003 August panel setting had a negligible effect on the gain during that period allowing us to assign a single constant efficiency for each observing season.

We measured the beam efficiency for the 2003 and 2004 seasons directly from planetary observations (see above), but no similar dataset exists for previous seasons. Therefore, we have attempted to determine the beam efficiency for the 2000–2004 seasons by comparing the intensities of spectral line observations of molecular cloud cores taken during different seasons. Table 7 shows the intensity ratios of the sources observed and the periods which they cover. We define the relative seasonal beam efficiency η_{yr} to be:

$$\eta_{\mathrm{yr}} \equiv \frac{T^*_{\mathrm{A,yr}}}{T^*_{\mathrm{A,2004}}} \qquad (5)$$

where $T^*_{\mathrm{A,yr}}$ is the antenna temperature measured in a given year and $T^*_{\mathrm{A,2004}}$ is the antenna temperature that would

Table 5. Telescope adjustments 2000–2004

Date	Adjustment
2000 Jan	subreflector adjustment
2000 May	collimation & focussing
2000 May	collimation & focussing
2002 Jun	subreflector adjustment
	collimation & focussing
2003 May	subreflector adjustment
	panel adjustment
	collimation & focussing
2004 May	subreflector adjustment

Table 6. Seasonal efficiencies

Period	η_{yr}	η_{xb} [86 GHz]	η_{xb} [115 GHz]
2004	1.00	0.65	0.55
2003	0.95	0.62	0.52
2002	0.80	0.52	0.44
2001	0.70	0.46	0.39
2000	0.63	0.41	0.35

have been measured had the observation been done during the 2004 season.

Since most of the observed sources are molecular cloud cores with extents greater or equal to $2'$, we assume that emission from these sources encompasses both the main beam and inner error beam at the frequencies observed. Therefore, we believe that η_{yr} quantifies how η_{xb} varied as a function of observing season. Equation 3 can then be written as follows:

$$T^*_{\mathrm{A,yr}} = \eta_{\mathrm{xb,2004}}\eta_{\mathrm{yr}} \frac{\int T_{\mathrm{R}}(\phi)\, P_{\mathrm{xb}}(\phi)\mathrm{d}\Omega}{\int P_{\mathrm{xb}}(\phi)\mathrm{d}\Omega} \qquad (6)$$

where $\eta_{\mathrm{xb,2004}}$ is the extended beam efficiency during the 2004 season, and $\eta_{\mathrm{xb,2004}}\eta_{\mathrm{yr}} = \eta_{\mathrm{xb,yr}}$ is the extended beam efficiency for a given season.

Using the measured year-to-year intensity ratios, we estimated the beam efficiency for each year, normalised to the 2004 observing season values. No source was observed during every observing season, so we adopted an indirect method for determining the relative gains that made use of each pair of observations. The relative efficiencies of all the observing seasons can be expressed as a five-element vector, (η_{2000}, η_{2001}, η_{2002}, η_{2003}, η_{2004}), with η_{2004} set to 1. Starting from an initial guess, the parameter space of potential model vectors was generated by numerically incrementing each element in steps of ± 0.05 over a suitable range. Each model was evaluated by comparing the model's predicted intensity ratios with the observed values. The reduced χ^2 value was calculated from each model based on this comparison. As our final vector of efficiencies we took the χ^2-weighted average of the models with χ^2 values from the minimum value (χ^2_{min}) to $\chi^2_{\mathrm{min}} + 1$. The results for the years 2000 to 2004 are shown in Table 6. An estimate of the error associated with the results was

Table 7. Cross period observations

| Source	Line	Period 1	Period 2	Period 1/Period 2
Orion KL	HCO$^+$	2000 Sep	2001 Oct	0.912 ± 0.011
	HCO$^+$	2000 Sep	2004 Jun	0.630 ± 0.003
	HCO$^+$	2001 Oct	2004 Jun	0.691 ± 0.008
M17SW	HCN	2000 Oct	2001 Aug	0.943 ± 0.009
	HCN	2000 Oct	2001 Aug	0.937 ± 0.005
	HCN	2000 Oct	2001 Aug	0.858 ± 0.005
	HCN	2000 Oct	2004 Jul	0.630 ± 0.003
	HCN	2001 Aug	2004 Jul	0.669 ± 0.006
	HCN	2001 Aug	2004 Jul	0.673 ± 0.004
	HCN	2001 Aug	2004 Jul	0.735 ± 0.004
	HCO$^+$	2000 Oct	2001 Aug	0.747 ± 0.003
	HCO$^+$	2000 Oct	2004 Jul	0.516 ± 0.003
	HCO$^+$	2001 Aug	2004 Jul	0.691 ± 0.003
OPH-EL21	C^{18}O	2002 Jul	2003 Aug	0.635 ± 0.029
CHA-B18	C^{18}O	2002 Jul	2003 Aug	1.057 ± 0.234
CHA-B35	C^{18}O	2002 Jul	2003 Aug	0.826 ± 0.077
CHA-C1-6	C^{18}O	2002 Jul	2003 Aug	1.096 ± 0.120
CHA-INA2	C^{18}O	2002 Jul	2003 Aug	1.067 ± 0.103
CHA-IRAS1107	C^{18}O	2002 Jul	2003 Aug	0.979 ± 0.143
CHA-IRAS1303	C^{18}O	2002 Jul	2003 Aug	0.838 ± 0.243
CHA-IRASF125	C^{18}O	2002 Jul	2003 Aug	2.098 ± 0.833
CHA-IRS11	C^{18}O	2002 Jul	2003 Aug	0.875 ± 0.093
CHA-IRS4	C^{18}O	2002 Jul	2003 Aug	0.757 ± 0.077
CHA-PERSI91	C^{18}O	2002 Jul	2003 Aug	0.775 ± 0.079
CRA-W97-1-26	C^{18}O	2002 Jul	2003 Aug	0.926 ± 0.067
L1527	C^{18}O	2002 Jul	2003 Aug	0.934 ± 0.059
G0.55-0.85	CH$_3$CN	2000 Sep	2003 Oct	0.788 ± 0.017
G5.90-0.43	HCN	2003 Oct	2004 Jun	0.834 ± 0.019
	HCN	2003 Oct	2004 Jun	0.802 ± 0.012
G10.32-0.16	HCN	2000 Oct	2003 Oct	0.895 ± 0.022
	HCN	2000 Oct	2004 Jun	0.641 ± 0.015
	HCN	2003 Oct	2004 Jun	0.717 ± 0.014
G10.47+0.03	CH$_3$CN	2002 Oct	2003 Oct	0.885 ± 0.013
G11.94-0.15	HCO$^+$	2001 Jul	2003 Oct	0.768 ± 0.029
G11.94-0.62	HCO$^+$	2000 Sep	2003 Oct	0.878 ± 0.021
G12.18-0.12	HCO$^+$	2001 Jul	2003 Oct	0.637 ± 0.017
	HCO$^+$	2001 Jul	2004 Jun	0.634 ± 0.026
	HCO$^+$	2001 Jul	2004 Jun	0.636 ± 0.037
	HCO$^+$	2003 Oct	2004 Jun	0.996 ± 0.040
	HCO$^+$	2003 Oct	2004 Jun	0.998 ± 0.056
G15.03-0.68	HCO$^+$	2001 Aug	2004 Jun	0.690 ± 0.005
	HCO$^+$	2001 Aug	2004 Jun	0.732 ± 0.011
	HCN$^+$	2000 Oct	2003 Oct	0.531 ± 0.003
G29.87-0.04	HCN	2000 Oct	2004 Jun	0.780 ± 0.014
	HCN	2000 Oct	2004 Jun	0.869 ± 0.015
G30.82-0.05	CH$_3$CN	2001 Aug	2003 Oct	0.688 ± 0.015

obtained from the standard deviation of the raw intensity ratios for each period and was approximately 20%.

4 Comparisons with Other Observatories

We compare efficiency-corrected Mopra observations with measurements of the same sources made at other facilities, namely the Five College Radio Astronomy Observatory (FCRAO) 14-m telescope in New Salem, USA, the Swedish–ESO Submillimetre Telescope (SEST) at La Silla, Chile, and the Institut de Radioastronomie Millimétrique (IRAM) 30-m telescope near Granada, Spain. These telescopes vary from two-thirds the size of Mopra to

50% larger, and so the FWHM size of their main beams differ from that of the Mopra main beam. The FWHM sizes of the 14-m FCRAO and 15-m SEST telescope main beams are 48″ and 45″ respectively, while the FWHM size of the IRAM 30-m telescope main beam is 24″ at the frequencies observed. The choice of filter banks lead to a similar velocity resolution of $\sim$0.1 km s^{-1} for all telescopes.

The spectra from the Mopra telescope and from the other facilities are shown in Figures 5 and 6. The sources observed with the FCRAO and IRAM telescopes consist of circumstellar material surrounding forming stars deeply embedded in the Taurus Molecular cloud, measured in the 110 GHz line of C^{18}O. The Mopra observations were
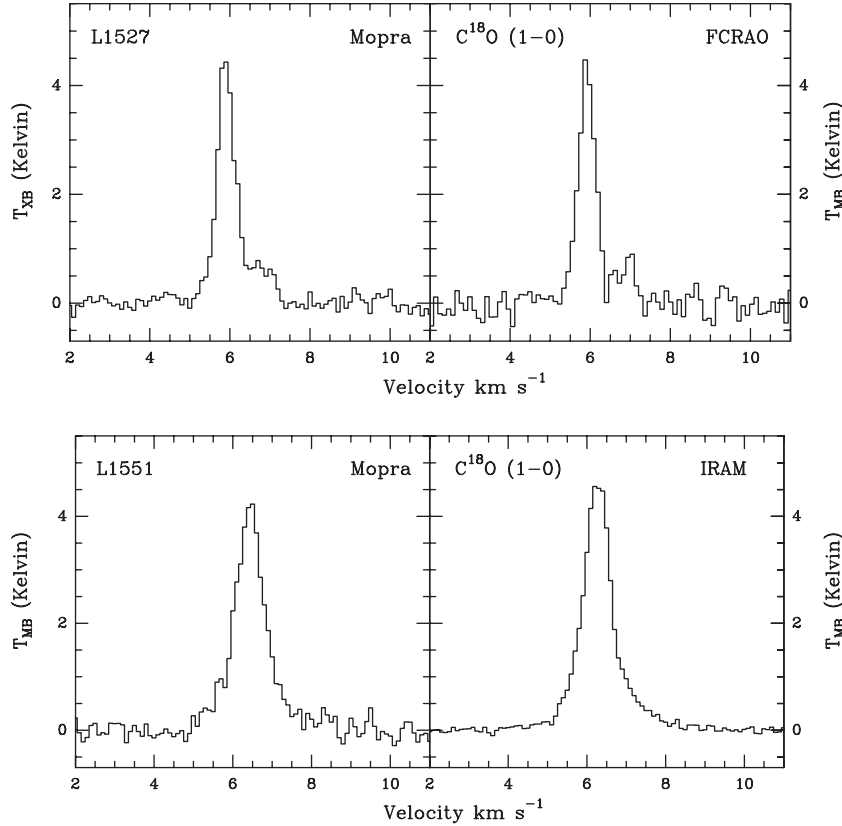
Figure 5   Efficiency-corrected $C^{18}O$ spectra of the molecular cores L1527 and L1551 acquired with the Mopra telescope (left panels) and the FCRAO and IRAM telescopes (right panels). The Mopra L1527 data have been calibrated onto an extended beam temperature scale using η_{xb} and the analogous FCRAO value for the FCRAO spectrum while the Mopra L1551 data have been calibrated onto a main beam temperature scale using η_{mb}.

acquired in 2003, while the FCRAO spectrum of L1527 was obtained in 1995, and the IRAM spectrum of L1551 was obtained in 1999. Observations of the nearby Orion-KL hot core with the SEST were acquired in as part of the calibration program in 1997[1], while the Mopra observations were were acquired during 2004 June.

The $C^{18}O$ emission in the region around L1527 is extended on scales larger than $2'$, and so the Mopra data were calibrated with the extended beam efficiency, η_{xb}. The FCRAO spectrum was calibrated onto a comparable temperature scale using the forward scattering efficiency measured by Ladd & Heyer (1996).

The $C^{18}O$ emission in the region around L1551 is more localised, and so calibration with the main beam efficiency, η_{mb} is more appropriate. The IRAM data for this source were calibrated onto the main beam temperature scale using the efficiencies quoted on the IRAM website (www.iram.es/).

In both cases, the correspondence between the Mopra data and the spectra from other facilities is quite good. The line shape, line centre velocity[2], and peak intensity

correspond well. The calibrated IRAM spectrum has a slightly higher peak temperature which probably results from the smaller FWHM beam size, and the fact that the intensity distribution is somewhat centrally peaked around this source.

Both the ^{12}CO and ^{13}CO emission in the Orion-KL region are extended on scales larger than an arcminute with the narrow spike feature of the spectrum attributed to the central source and the broad linewings to the associated bipolar outflow (e.g. Gillespie & White 1980). Both features are assumed to couple well to the extended beam and are calibrated onto the T_{xb} temperature scale. The SEST beam at $45''$ FWHM is calibrated onto the equivalent SEST T_{mb} using the efficiencies quoted in the SEST observers manual[3].

Maps of Orion KL in the 89 GHz transition of HCN (cf. Rydbeck et al. 1981) show the emission to be localised to the central $20''$, so calibration of the Mopra HCN data with the main beam efficiency is more appropriate. The spectra from both facilities have similar shapes

---

[1] SEST calibration data was provided courtesy of the Onsala Space Observatory and Chalmers University of Technology.

[2] During and before the 2003 observing season, some Mopra data suffered from a frequency calculation error that resulted in spectra which appeared shifted in frequency by as much at 500 kHz. The source of

this error has been identified, and all data can be corrected to a proper frequency scale with a simple algorithm. See http://narrabri.atnf.csiro.au/mopra for details.

[3] The SEST observers manual, maintained by Markus Nielbock, is available online www.ls.eso.org/lasilla/Telescopes/SEST/SEST.html
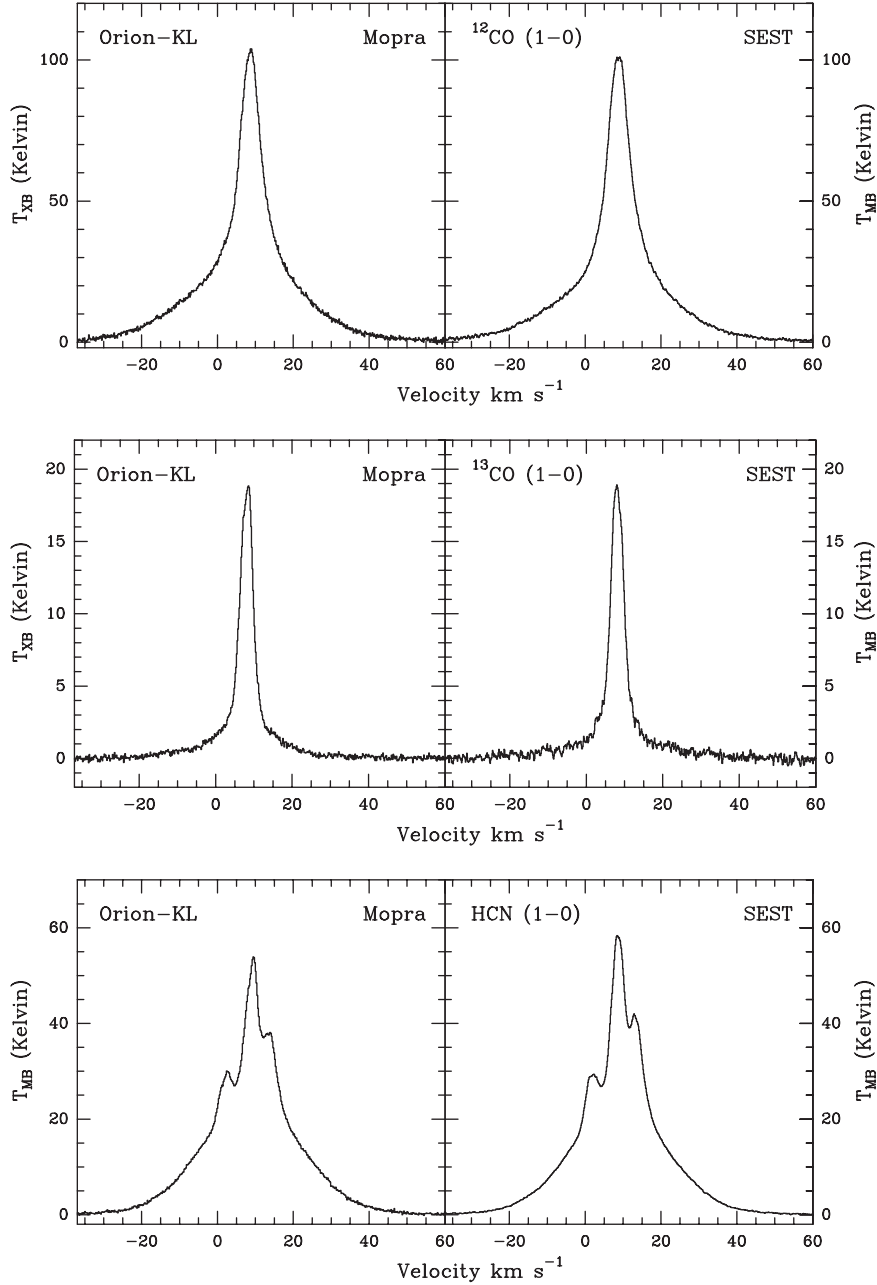
Figure 6 Efficiency-corrected ^{12}CO, ^{13}CO, and HCN spectra of the molecular core Orion-KL taken with the Mopra telescope (left panels) and the SEST 15-m telescope (right panels). The CO data have been calibrated onto an extended beam temperature scale using η_{xb} and the analogous SEST value for the SEST spectrum while the Mopra HCN data have been calibrated onto a main beam temperature scale using η_{mb}. Integration times have not been matched across linepairs.

and intensities. Peak intensities agree to within 10%, well within the expected calibration uncertainty of the single load calibration method employed at Mopra.

5 Standard Spectra

M17-SW and Orion-KL are commonly used as calibrators in millimetre-line spectroscopy due to the high intensity of observed molecular transitions and their relatively large angular extent compared to modern telescope beams at 3-mm wavelengths. We present high SNR spectra toward

both sources in Figure 7, taken in a number of abundant molecular species. The coordinates used are the same as those quoted by other millimetre and sub-millimetre telescopes, such as the SEST, so a direct comparison may be made. A digital auto-correlator having a bandwidth of 64 MHz divided into 1024 channels formed the back-end, delivering a velocity resolution of less than $0.3 \, \text{km s}^{-1}$. Care was taken to reduce the pointing error while observing to $<5''$ by reference pointing on a nearby bright SiO maser, or, in the case of Orion, its own associated maser.
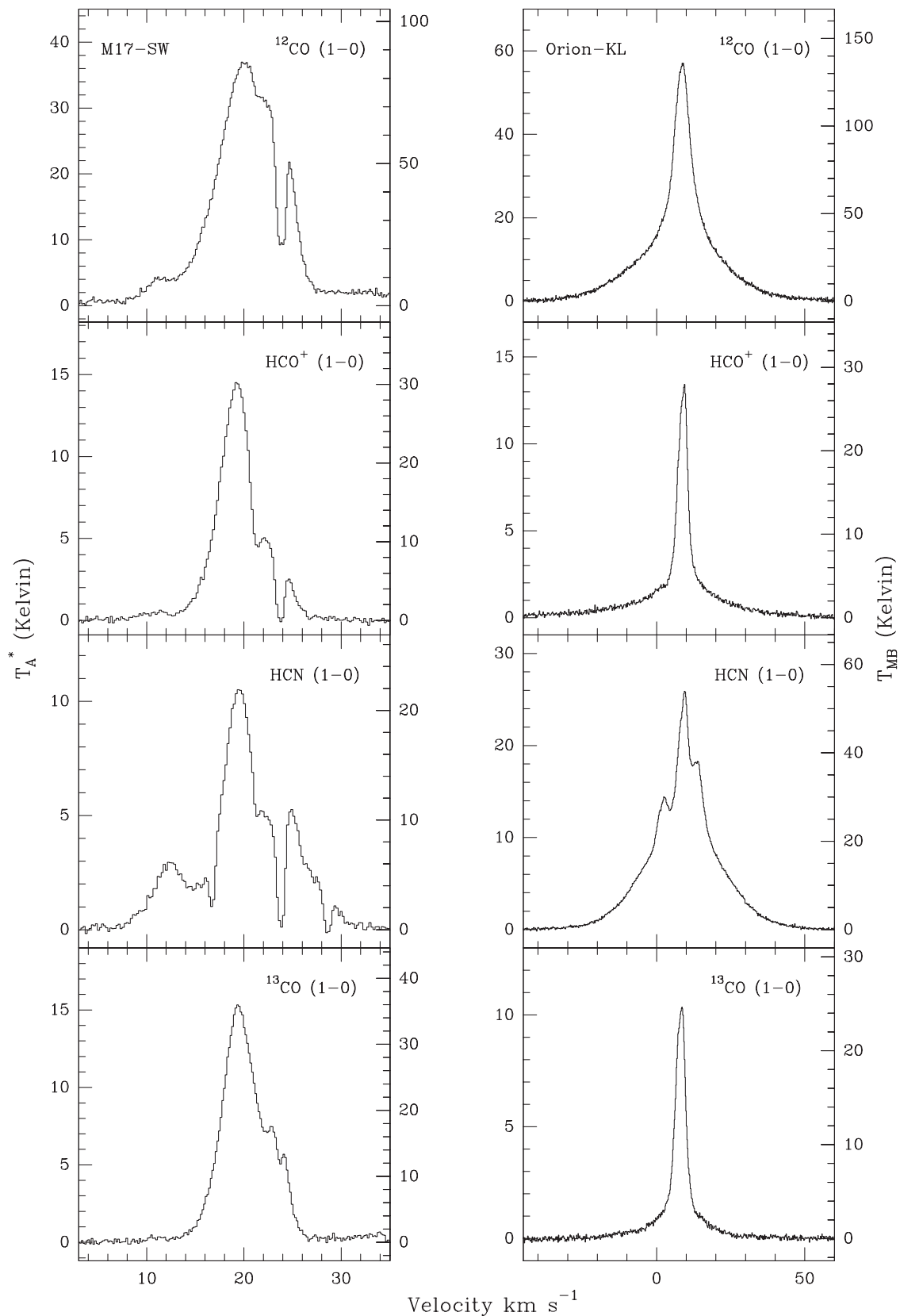
Figure 7   Standard spectra towards M17-SW and Orion-KL. The following coordinates were used in all observations: Orion-KL – $05^h35^m14.5^s$, $-05°22'29.6''$ (J2000.0), and M17-SW – $18^h20^m23.1^s$, $-16°11'37.2''$ (J2000.0). The left y-axis displays T_A^* and the right y-axis T_{mb}, corrected for the main beam efficiency at the frequency of the line.

6 Summary and Conclusions

We present measurements of the beam size, shape, and beam efficiency of the 22-m ATNF Mopra Radio Telescope in the frequency range 86–115 GHz. The main beam of the telescope is well-fit out to an angular offset of $40''$ by a Gaussian with FWHM size of $36 \pm 3''$ at frequencies below 100 GHz and FWHM size of $33 \pm 2''$ at a frequency of 115 GHz. The telescope's beam also contains a lower level error beam which extends to angular offsets of $80''$ with an average response of less than 2% of peak response.

The data indicate a main beam efficiency, η_{mb} which ranges from 0.49 at 86 GHz to 0.42 at 115 GHz, and an extended beam efficiency, η_{xb} which ranges from 0.65 to 0.55 over the same frequency range. Comparisons with observations taken during previous observing seasons indicate that these efficiencies have been dramatically improved by modifications to the telescope structure. Estimates for the value of η_{xb} during previous observing seasons are presented.

We also present observatory standard spectra taken in several spectral lines toward two well-known sources. Observers may wish to compare their observations to these spectral standards to evaluate the state of the telescope system during their observing runs.

References

Epstein, E. E., & Andrew, B. H. 1985, Icar, 62, 448

Gillespie, A. R., & White, G. J. 1980, A&A, 91, 257

Kutner, M. L., & Ulich, B. L. 1981, ApJ, 250, 341

Ladd, E. F., & Heyer, M. H. 1996, FCRAO Technical Memorandum (Amherst MA: University of Massachusetts)

Mangum, J. G. 1993, PASP, 105, 117

Moorey, G. G., Sinclair, M. W., & Payne, J. M. 1997, in IAU Symposium 170, CO: Twenty-Five Years of Millimeter-Wave Spectroscopy, eds. W. B. Latter et al., 441

Neugebauer, G., Munch, G., Kieffer, H., Chase, Jr., S. C., & Miner, E. 1971, AJ, 76, 719

Rydbeck, O. E. H., Hjalmarson, A., Rydbeck, G., Ellder, J., Olofsson, H., & Sume, A. 1981, ApJ, 100, 30

Ulich, B. L. 1981, AJ, 86, 1619

Wilson, W. E., Davis, E. R., Loone, D. G., & Brown, D. R. 1992, JEEEA, 12, 187